



Efficient CO₂ reduction to reveal the piezocatalytic mechanism: From displacement current to active sites

Zhuoran Ren^{a,1}, Fang Chen^{b,1}, Qin Zhao^{a,*}, Guoqiang Zhao^c, Hui Li^d, Wenping Sun^c, Hongwei Huang^{b,*}, Tianyi Ma^{d,*}

^a Institute of Clean Energy Chemistry, Key Laboratory for Green Synthesis and Preparative Chemistry of Advanced Materials, College of Chemistry Liaoning University, Shenyang 110036, PR China

^b Beijing Key Laboratory of Materials Utilization of Nonmetallic Minerals and Solid Wastes, National Laboratory of Mineral Materials, School of Materials Science and Technology, China University of Geosciences, Beijing 100083, PR China

^c School of Materials Science and Engineering, State Key Laboratory of Clean Energy Utilization, Zhejiang University, Hangzhou 310027, PR China

^d School of Science, RMIT University, Melbourne, VIC 3000, Australia

ARTICLE INFO

Keywords:

Piezocatalytic CO₂ reduction reaction
Piezocatalytic mechanism
Displacement current and the principle of PENG
Design of piezocatalyst

ABSTRACT

Piezocatalysis has attracted the increasing interest of researchers as a novel catalytic method. To date, there are two popular mechanisms regarding the piezocatalysis, i.e., the piezoelectric effect and the energy band theory. However, both mechanisms cannot fully explain the piezocatalytic process: the electrons generated by the piezoelectric effect will not spontaneously participate in the piezocatalysis, while not all piezoelectric materials have an appropriate energy band structure. In this work, displacement current and the principle of piezoelectric nanogenerator are introduced to fully comprehend the piezocatalytic mechanism for the first time. As a proof-of-concept catalytic system, we synthesize Co-N-C@BaTiO₃ piezocatalyst for the CO₂ reduction reaction (CO₂RR) under ultrasonic vibration. A promising piezocatalytic CO₂ reduction rate of 261.8 mol g⁻¹h⁻¹ is achieved with a high CO selectivity up to 93.8% under 50 kHz ultrasonic vibration. The CO yields of this catalytic system outperform most of the reported photocatalytic CO₂RR and piezocatalytic CO₂RR. Moreover, a comprehensive piezocatalytic mechanism from displacement current to active sites is proposed and supported by combining Co-N-C@BaTiO₃ piezoelectric nanogenerator, COMSOL simulation and energy band structure analysis. Under the ultrasonic vibration, the electrons generated by the piezoelectric effect are driven by the time-varying electrostatic potential formed by the displacement current. The suitable band structure of piezoelectric provider that satisfies the potential of reaction promotes electrons to participate in CO₂RR on active sites. Overall, our work provides an insightful understanding of piezocatalysis and paves a new path for its development.

1. Introduction

Piezoelectric materials have already been discovered over a hundred years. [1] However, applications of piezoelectric materials in the field of catalysis have just received attention. Unlike thermocatalysis, electrocatalysis, and photocatalysis, piezocatalysis utilize the piezoelectric properties of piezoelectric materials to convert mechanical energies into electrical energy for the catalytic reaction. [2,3] The invention of piezoelectric nanogenerator (PENG) by Wang et al. set off a research upsurge in piezoelectric materials, [4] while the abundant mechanical energies, e.g., ocean wave, [5] vibrations, [6] droplet, [7] ball milling,

[8] and human breathing, [9] also provides more opportunities for realizing piezocatalysis. Therefore, it is important to study the piezocatalytic mechanism. From the current research, the piezocatalytic mechanism can be roughly divided into piezoelectric effect and energy band theory. [2,3,10,11] The piezocatalytic mechanism based on piezoelectric effect believes that piezocatalysts use the mechanical energy obtained from the environment to convert into electrical energy to participate in the reaction. [12] However, the electrons accumulated on the surface of piezoelectric materials by the piezoelectric effect may not spontaneously participate in the catalytic reactions. According to displacement current and the principle of piezoelectric nanogenerator,

* Corresponding authors.

E-mail addresses: zhaoqin@lnu.edu.cn (Q. Zhao), hwh@cugb.edu.cn (H. Huang), tianyi.ma@rmit.edu.au (T. Ma).

¹ These authors contributed equally.

the electrons are driven by a time-varying electrostatic potential. [13] While, the piezocatalytic mechanism based on energy band theory employed the semiconductor properties of piezoelectric semiconductor materials and to propose that the mechanical energy such as ultrasonic vibration can directly excite the electrons from valence band (VB) to conduction band (CB) to participate the piezocatalysis. [3,14,15] However, not all piezoelectric materials have an appropriate energy band structure. Larger band gaps in piezoelectric semiconductor materials may not excite enough electrons to participate in the reaction [16]. Besides, not all piezoelectric materials, e.g., poly(vinylidene fluoride) (PVDF) and poly(tetrafluoroethylene) (PTFE), have semiconducting properties. [17,18] If the energy band theory is utilized to explain the piezocatalytic mechanism, the suitable band structure of piezoelectric semiconductor materials should be considered primarily based on the different reaction potential requirements. Therefore, the existing two dominant mechanisms cannot fully explain the piezocatalysis process, limiting the application potential of piezocatalysis.

Currently, the piezocatalysis is mainly applied in piezoelectric pollutants degradation and piezoelectric hydrogen production. [14, 19–24] The investigation of piezocatalytic CO₂ reduction reaction (PCO₂RR) has received negligible attention because the activation and reduction of CO₂ are difficult, compared with degradation and hydrogen production, which is more challenging in piezocatalysis. [25,26] Owing to the high economic value of carbon products and the environmental protection requirements of the carbon cycle. Nevertheless, the piezocatalysis still has its unique advantages in CO₂RR as compared with extensively explored thermocatalytic CO₂RR, photocatalytic CO₂RR, and electrocatalytic CO₂RR. [27–33] The PCO₂RR can be carried out under mild conditions is safer and more eco-friendly compared with the harsh reaction conditions and severe pollution in thermocatalytic CO₂RR [34]. Furthermore, it can also reduce or avoid the usage of sacrificial agents and complete the CO₂RR without light, compared with photocatalytic CO₂RR. [20, 35–37] Besides, the PCO₂RR utilizes mechanical energies from the environment, leading to the energy cost being more competitive than the high electric energy consumption in electrocatalytic CO₂RR. Therefore, PCO₂RR provides more possibilities and options for realizing carbon neutralization. [38] The design of piezocatalyst is particularly important to realize PCO₂RR. The piezocatalysts are mainly designed by modulating the piezoelectric properties of piezocatalysts, while the design of catalytic active sites has been ignored thus far. However, appropriate catalytic active sites are crucial to improve the activity and the selectivity of target products in CO₂RR. Therefore, the piezocatalysts should possess not only excellent piezoelectric properties but also appropriate active sites.

In this work, we propose a comprehensive mechanism of piezocatalysis by introducing the displacement current and the principle of PENG into the two popular piezocatalytic mechanisms. [3,11,13] As a proof-of-concept piezocatalytic system, we synthesized a Co-N-C@BaTiO₃ (Co-N-C@BTO) piezocatalyst for PCO₂RR. In order to realize PCO₂RR efficiently, Co-N-C is employed as the active sites which demonstrated an excellent catalytic activity and selectivity in the study of electrocatalytic CO₂RR [39,40]. Meanwhile, Co-N-C also has an excellent stability and conductivity which facilitates enhanced charge separation [41]. BTO is selected as a piezoelectric provider due to its excellent piezoelectric response and a suitable band structure for CO₂RR. [20,24,42] Co-N-C@BTO piezocatalyst successfully converts CO₂ into CO at room temperature under ultrasonic vibration. It is worth mentioning that the yield of CO using Co-N-C@BTO piezocatalyst is superior to that of most photocatalytic CO₂RR and PCO₂RR. [31,43] Furthermore, the displacement current and the principle of PENG in PCO₂RR are also investigated by Co-N-C@BTO PENG, COMSOL simulation and energy band structure analysis. This work provides a comprehensive understanding of piezocatalytic mechanism from displacement current to active sites and sheds light on the practical application of piezocatalysis.

2. Experimental section

2.1. Materials

The raw materials of Zn(NO₃)₂·6 H₂O, Co(NO₃)₂·6 H₂O, and 2-methylimidazole were purchased from Aladdin Co., Ltd. BTO powder, KHCO₃ and methanol were purchased from Macklin Biochemical Co., Ltd. All chemicals were analytically pure used without further purification.

2.2. Synthesis of Co/Zn-ZIF

Zn(NO₃)₂·6 H₂O (5.948 g) and Co(NO₃)₂·6 H₂O (2.909 g) were dissolved in 100 mL methanol. After that, 2-methylimidazole (6.16 g) was dissolved in 100 mL methanol. Then, the 2-methylimidazole solution was subsequently dropped into the above solution under vigorously magnetic stirring for 6 h at room temperature and stayed still for over 24 h. As obtained precipitates were collected by centrifugation at 11000 rpm for 5 min, washed three times with methanol, and finally freeze-dried in a vacuum at −40 °C maintained for 12 h.

2.3. Synthesis of Co-N-C

The powder of Co/Zn-ZIF was put in a tube furnace, under the flowing Ar gas, with a heating rate of 10 °C/min from room temperature, after that it kept at 800 °C for 1 h, 900 °C for 1 h with a heating rate of 5 °C/min, and 1000 °C for 2 h with a heating rate of 2 °C/min. And then let it naturally cooled to room temperature.

2.4. Synthesis of Co-N-C@BTO

Co-N-C (0.1 g) mixed with BTO (2 g) were placed into the agate jar with some agate ball mill beads. Fixed the agate jar into the planetary ball milling machine, after that initiated the ball milling with 480 rpm for 12 h.

2.5. Material characterization

The crystal structure of the powder was characterized using a Bruker D8-Advance with Cu K α radiation (λ = 0.15406 nm, 40 kV and 15 mA). The morphologies of material were characterized by transmission electron microscopy (TEM, JEOL 2100 F, Japan). The scanning electron microscope (SEM) was carried out by a SU8010 and energy dispersive EDS mapping (APOLLO.XL, EDAX company, USA). The Co atomic dispersion of catalyst was tested by scanning transmission electron microscopy (FEI Titan G² 80–200 ChemiSTEM USA). X-ray photoelectron spectroscopy (XPS, ESCALAB 250Xi, thermos, USA) was used to analyze the chemical composition of material. The binding energies of elements were corrected by using C 1 s peak at 284.8 eV of contaminant carbon as a reference. Piezoresponse force microscopy (PFM, AFM multi-Mode-8, Bruker, Germany) was used to investigate the piezoelectric properties of piezocatalyst. Adsorption isotherm curve and pore width of material were tested by Micromeritics TriStar II 3020. The finite element method (FEM) calculations were performed using COMSOL Multiphysics 5.4 with the module of the piezoelectric device based on the steady-state study. The physicochemical parameters of BTO were assigned by COMSOL material database. The gas product was quantified by Gas Chromatography (GC, SP-3400, BFRL, China), H₂ was analyzed by thermal conductivity detector (TCD) and CO was analyzed by flame ionization detector (FID).

2.6. Piezocatalytic CO₂RR and gas product testing

The piezocatalytic CO₂RR and product testing process was illustrated in schematic S1. This work utilized food-grade pure CO₂ as a gas source, and an ultrasonic washing machine as a mechanical energy source with

different frequencies (25 kHz, 50 kHz, 75 kHz, and 100 kHz). The temperature of the ultrasonic bath was controlled at 20 °C (± 0.5 °C) by circulating water through an external cooling bath during the reaction time. The reactor was a sealed cylindrical glass reactor with a volume of 600 mL. 40 mg of Co-N-C@BTO powder was added and dispersed into a

500 mL of 0.1 M KHCO_3 (pH=8.57) solution. The solution was then saturated with CO_2 . No sacrificial agent was used in this process. The solution is already saturated with CO_2 before each time piezocatalytic CO_2RR . Therefore, the strength of the ultrasound microbubbles should mainly depend on the different frequencies of the vibrating devices of

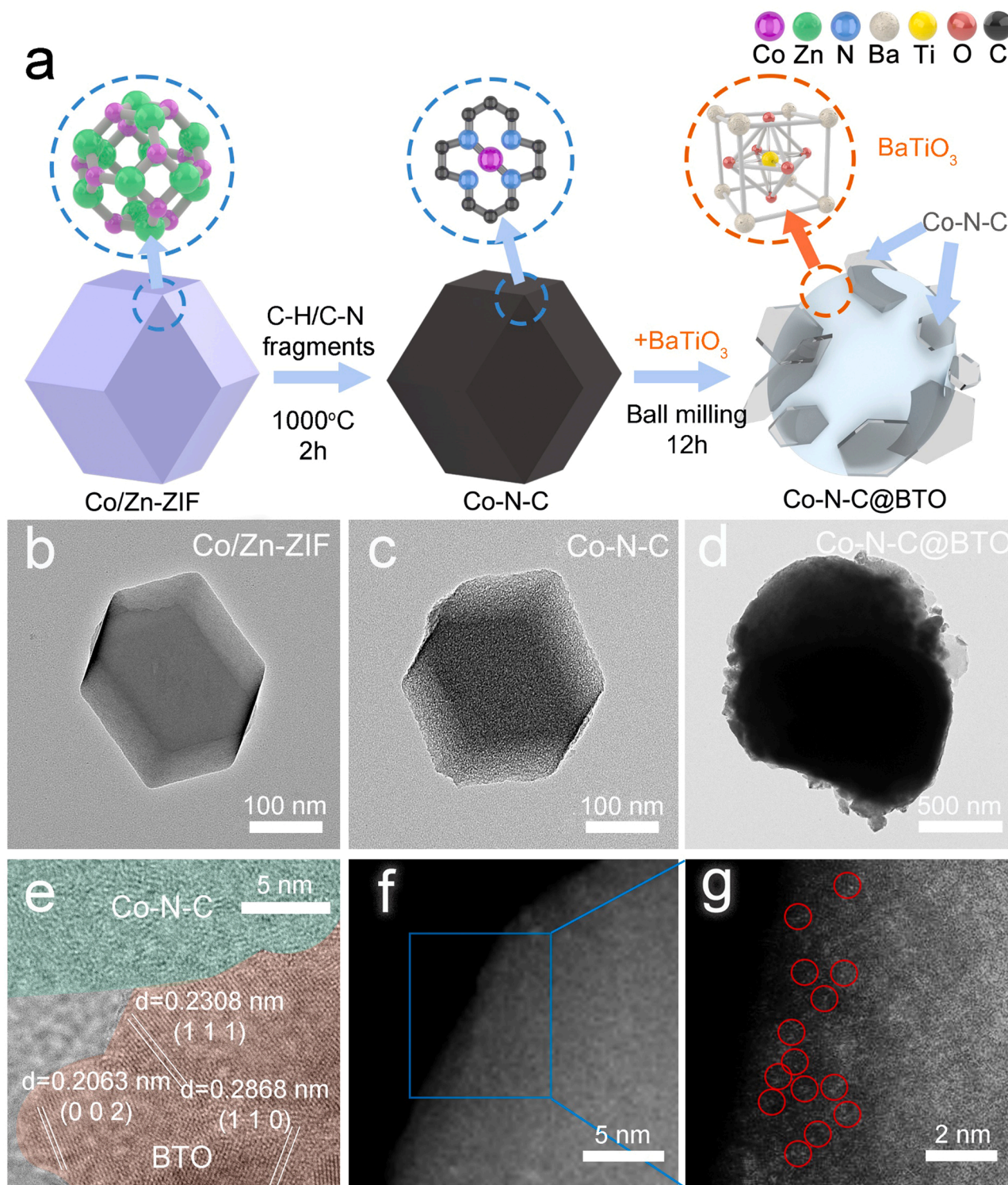


Fig. 1. Synthesis process and morphology of Co/Zn-ZIF, Co-N-C, and Co-N-C@BTO. (a) Schematic of the Co-N-C@BTO synthesis process. (b) The TEM image of Co/Zn-ZIF shows a dodecahedron shape. (c) The TEM image of Co-N-C keeps a good morphology after 1000°C calcination. (d) The TEM image of Co-N-C@BTO illustrates that Co-N-C is crashed into nanoparticles that combined with BTO with a broken morphology after the ball-milling process. (e) The high-resolution TEM of Co-N-C@BTO shows the interface between them and the lattice finger proves the existence of BTO, which proves a strong combination between Co-N-C and BTO. (f, g). The magnified HAADF-STEM picture of Co-N-C@BTO shows atomically dispersion of Co ions.

the ultrasound washing machine and without being influenced by the degree of dissolution of the gas. Then sealed the reactor and put it in the center of ultrasonic washing machine. Next, turn on the ultrasonic under fixed frequency (25 kHz, 50 kHz, 75 kHz, or 100 kHz) for 1 h. After that, the gas products were collected by gas sampling bag (1 L) and injected into gas chromatography for detection. The gas chromatography with FID and TCD as gas product detectors. Argon was used as a carrier gas to enhance the sensitivity of hydrogen detection. H_2 , N_2 and air gas were used to separate other carbon based products. Quantification of the gas product was conducted using BFRL Software based on the calibration curves, which were previously determined by using different concentrations of H_2 , CO and other carbon based products.

2.7. Assembling PENG and piezoelectric current test

In Schematic S2, a PENG device was assembled by using Co-N-C@BTO as the negative electrode and the positive electrode. For preparing Co-N-C@BTO electrodes, Co-N-C@BTO, super P and Polyvinylidene fluoride (PVDF) were mixed with N-methylpyrrolone (NMP) with weight ratio of 8: 1: 1. The slurry was painted on Cu foils and dried at 80 °C overnight in vacuum oven. A piece of cellulose paper as a separator were soaked in a 0.1 M $KHCO_3$ electrolyte for 5 min. The PENG device was wrapped and sealed with aluminum plastic film to prevent electrolyte from drying. Battery sealing machine for sealing PENG (Secondary turntable vacuum packaging machine, GRS-FZ200, Wuhan Grace New Energy Co., Ltd.). Piezoelectric current was measured using an electrochemical workstation. PENG was placed in an ultrasonic washing machine and placed vertically. Piezoelectric ultrasonic vibration was supplied by an ultrasonic washing machine with a power of 300 W and frequencies of 25 kHz, 50 kHz, 75 kHz, and 100 kHz (SB-300DXY, Ningbo SCIENTZ biotechnology. Co. LTD, China). It was sampled by chronoamperometry method for 1 min under each different frequency. The chronoamperometry curves were tested by an electrochemical workstation (Shanghai Chen-Hua CHI660, China).

3. Results and discussion

3.1. Piezocatalyst synthesis and characterization

Fig. 1a illustrates the synthetic process of Co-N-C@BTO piezocatalyst. The Co/Zn zeolitic imidazolate frameworks (Co/Zn-ZIFs) are employed as the precursor to synthesize Co-N-C by pyrolysis. The Co-N-C@BTO piezocatalyst is prepared by mixing Co-N-C with BTO under ball milling. This synthetic method could obtain a gram level yield (Fig. S1). The crystal phase of Co/Zn-ZIF, Co-N-C, BTO and Co-N-C@BTO is confirmed by X-ray diffraction (XRD). The diffraction peaks of Co/Zn-ZIF are matched with ZIF-67 (Fig. S2), [39,40,44,45] while the Co-N-C shows an amorphous form, which is consistent with the corresponding selected area electron diffraction patterns (SAED) (Fig. S3, Fig. S4). Because of the low content of Co, no apparent Co metal peak is observed which corresponds to the corresponding energy-dispersive spectroscopy (EDS) mapping results (Fig. S5). [39] The diffraction peaks of Co-N-C@BTO in Fig. S6 can be assigned to the tetragonal BTO with a space group of $P4mm$ (JCPDS card no. 05-0626) (Fig. S7). No apparent change is observed in the XRD pattern after ball milling.

Figs. 1b, 1c, and 1d illustrate the transmission electron microscope (TEM) images of Co/Zn-ZIF, Co-N-C, and Co-N-C@BTO, respectively. The Co/Zn-ZIF exhibits a typical dodecahedron structure, and the morphology of Co/Zn-ZIF is remained after the calcination, indicating the Co-N-C has excellent structural strength (Fig. 1c). However, the surface of Co-N-C is not as smooth as Co/Zn-ZIF. There are abundant micropores after the high-temperature treatment due to the fragment of C-H bonds and C-N bonds in Co/Zn-ZIF. The adsorption isotherm further reveals the micropore structure of Co-N-C (Fig. S8 and Table S1), and the average pore width is about 0.48 nm (CO_2 kinetic diameter is about 0.33 nm in gas status). [46,47] It might be hard for the efficient

absorption of reactant through such small micropores, while the densified micropore structure makes the inside active sites of Co-N-C hardly utilized efficiently. [48] For this reason, the ball milling method is utilized to crash the Co-N-C into nanoparticles and combine it with BTO, which could simultaneously improve the utilization of active sites of Co-N-C (Fig. 1d). [49–51] After the ball milling process, the adsorption isotherm hysteresis loop cannot be generated by the adsorption curve and desorption curve (Fig. S9) which demonstrates the structure has already been destroyed, as is proved by the TEM image of Co-N-C@BTO in Fig. 1d. The Zn, Co, N, and C element distribution of Co-N-C is revealed by EDS mapping. After the calcination, it is obvious that the weight content of Zn is declined, and the weight content of Co remains unchanged (Fig. S10, Fig. S5, and Table S2). Since Zn will be evaporated away (b. p. 907 °C) and Co ions will be reduced by carbonized organic linkers during the pyrolysis process, leaving atomically dispersed Co ions anchored on nitrogen-doped porous carbon. [39,40] The aberration-corrected high-angle annular dark-field scanning transmission electron microscope (HAADF-STEM) with the sub-angstrom resolution is employed to directly observe the atomic dispersion of Co ions in Co-N-C (Fig. S4). The SAED pattern displays a dispersion ring, and high-resolution TEM (HRTEM) images show no lattice fringe, highlighting the amorphous structure of Co-N-C (Fig. S3).

The TEM and SAED patterns of BTO reveal the lattice structure of BTO with clearly lattice diffraction spots and lattice fringe (Fig. S11). The HRTEM image of Co-N-C@BTO demonstrates the combination between BTO and Co-N-C after the ball milling (Fig. 1e). The diffraction spot and the dispersion ring shown in SAED pattern also indicate the composition of Co-N-C and BTO (Fig. S12). The Co, N, and C elements are evenly distributed on BTO from the image of EDS mapping (Fig. S13). The HAADF-STEM EDS mapping confirms the distribution situation between Co-N-C and BTO in Co-N-C@BTO (Fig. S12). The HAADF-STEM images shown in Figs. 1f, 1g prove that Co-N-C@BTO piezocatalyst with atomically dispersed Co ions are successfully prepared by the ball milling method, and more Co-N-C active sites can be exposed, thereby improving the catalytic performance.

High-resolution X-ray photoelectron spectroscopy (XPS) spectra of Co-N-C are shown in Fig. 2a–c. For the Co 2p XPS spectrum (Fig. 2a), the Co 2p_{3/2} and Co 2p_{1/2} peaks at 779.7 eV and 794.69 eV could be ascribed to Co^{2+} , while those at 784.36 eV and 799.35 eV are attributed to the satellite peaks of Co^{2+} . Those results demonstrate the oxidation state of Co in Co-N-C is + 2. In the high-resolution N 1s spectrum (Fig. 2b), three strong peaks located at 398.4 eV, 399.63 eV, and 401.01 eV could be assigned to pyridinic-N, pyrrolic-N, and graphitic-N, respectively. It is obvious that the content of pyridinic-N dominates, indicating that the Co-N-C structure has been successfully synthesized and Co-N-C can serve as the high-performance active sites of CO_2RR . The peaks located at 284.8 eV, 285.74 eV, and 288.3 eV are attributed to the C-C bond, C-N bond, and C=O bond, respectively, as is displayed in the XPS spectrum in Fig. 2c. XPS spectra of Ba 3d, Ti 2p, and O 1s for pristine BTO and Co-N-C@BTO are also evaluated. For the XPS spectrum of pristine BTO, the peaks located at 778.28 eV and 793.58 eV are attributed to the Ba 3d_{5/2} and Ba 3d_{3/2} (Fig. 2d). In the Ti 2p spectrum, two strong peaks located at 457.82 eV and 463.52 eV can be assigned to Ti 2p_{3/2} and Ti 2p_{1/2}, respectively (Fig. 2e). According to Fig. 2f, the binding energies of O 1s peaks are divided into two components at 528.97 and 530.83 eV, which are attributed to the lattice oxygen (lattice O) and the bonded oxygen (bonded O) present in BTO crystals, respectively. Compared with pristine BTO, the Ba 3d, Ti 2p, and O 1s peaks of Co-N-C@BTO are slightly shifted to higher binding energies and the binding energy shift value is about 1 eV. The main peaks for Ba 3d_{5/2} and Ba 3d_{3/2} are shift to 779.29 eV and 794.59 eV (Fig. 2d), and in the XPS spectrum of Ti 2p, the peaks of Ti 2p_{3/2} and Ti 2p_{1/2} are shift to 457.82 eV and 463.52 eV (Fig. 2e), and lattice O and bonded O peak of O 1s are shift at 530.11 eV and 531.75 eV. The XPS spectra in Fig. 2d–f reveal the BTO is combined with Co-N-C which forms a robust binding force after ball milling. [8,15,39] It also indicates BTO combined with

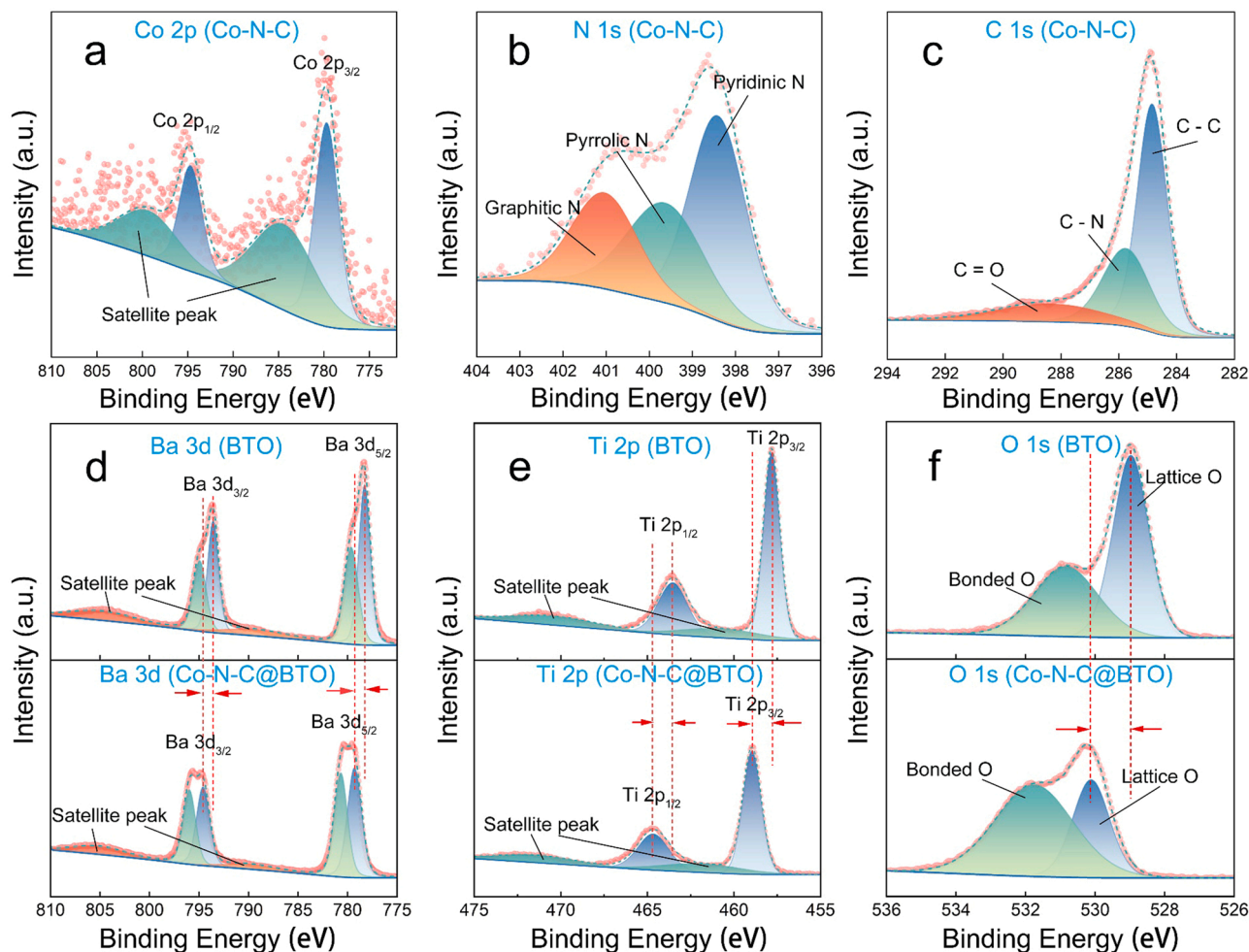


Fig. 2. High-resolution XPS spectra for Co-N-C, and comparison of the binding energy of Ba 3d, Ti 2p, and O 1s in BTO and Co-N-C@BTO. (a) In the XPS spectrum of Co 2p for Co-N-C, the signal-noise ratio of it reveals that the content of Co is low. (b) The XPS spectrum of N 1s for Co-N-C shows the Co has already formed Co-N coordination. (c) The XPS spectrum of C 1s for Co-N-C, (d)-(f) The comparison of XPS spectrum of Ba 3d, Ti 2p and O 1s.

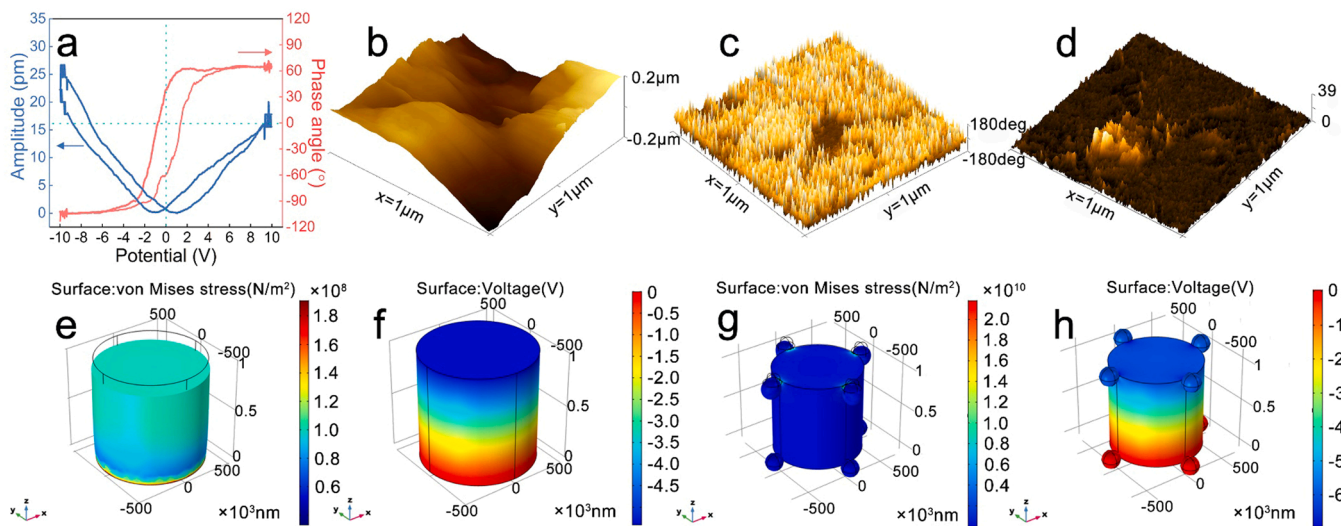


Fig. 3. Piezoelectric properties of Co-N-C@BTO and COMSOL simulations on BTO and Co-N-C@BTO under the stress process with Z-axis. (a) The phase-potential hysteresis loops (red line) and amplitude-potential butterfly loops (blue line) (b) The PFM 3D image of the morphology of Co-N-C@BTO. (c) The 3D phase image of Co-N-C@BTO. (d) The 3D vertical piezoelectric response amplitude of Co-N-C@BTO. (e) The stress on BTO along the Z-axis. (f) The piezoelectric potential upon the surface of BTO. (g) The stress on Co-N-C@BTO along the Z-axis. (h) The piezoelectric potential upon the surface of Co-N-C@BTO.

Co-N-C is steady enough for the ultrasonic vibration.

The piezoelectric properties of the Co-N-C@BTO are studied by the piezoelectric response force microscopy (PFM). The phase potential-hysteresis loop (red line) and the amplitude-potential butterfly loop (blue line) in Fig. 3a provide convincing evidence for the piezoelectric properties of Co-N-C@BTO. Based on the phase-potential hysteresis loops measured by the PFM, it could be observed that the remnant polarization is about 50 degrees and the piezoelectric domain angle exhibit a 160° change under the reversal by applying a voltage loop from -10–10 V, which exhibits an excellent piezoelectric domain rotate ability. According to the amplitude-potential butterfly loops, the maximum amplitude of Co-N-C@BTO is around 16 ~ 27 pm under 10 V, which confirms a promising piezoelectricity of the Co-N-C@BTO. Meanwhile, Fig. 3b shows the 3D view of Co-N-C@BTO surface morphology, displaying a rough height signal and the detailed surface of Co-N-C@BTO. The surface roughness of the Co-N-C@BTO is also presented which is approximately 200 nm. The straightforward contrast in the phase images indicates that the direction vector of the electric domain array is almost unity (Fig. 3c). Furthermore, based on the inverse piezoelectric effect, the amplitude image shows a strong piezoelectric response has been generated (Fig. 3d). The PFM results indicate that the Co-N-C@BTO exhibits a promising piezoelectric response. To further investigate and compare the piezoelectric properties of Co-N-C@BTO and BTO. The COMSOL simulation is utilized to simulate the piezoelectric properties of them. The morphology of Co-N-C@BTO are irregular after ball milling. The morphology of Co-N-C and BTO have already been broken. Therefore, during the process of COMSOL simulation, we have only idealized the model with reference to the account the average size of catalyst samples and a number of related studies[52]. For the convenience of general understanding, BTO with irregular morphology is equivalent to a cylinder (Figs. 3e, 3f), and the Co-N-C particles are equivalent to a nanosphere (Figs. 3g, 3h). The geometrical characteristics of the BTO model are set to a radius of 500 nm, a height of 1000 nm, and the Co-N-C model has a radius of 100 nm. The bottom surface of the model is fixed and grounded, a 100 MPa (the pressure inside a water bubble) compressive stress is applied to the

upper surface along the negative z-axis, they are also introduced to simulate the deformation (Fig. 3e) and piezoelectric potential (Fig. 3f) of BTO [52]. In the COMSOL simulation process, all the parameter are obtained from the COMSOL database. The simulated maximum potential (Table S3) of BTO indicate that the generated potential outputs are about -5.40 V on the surface of BTO. Similarly, the simulated maximum potential of Co-N-C@BTO (Table S4) shows that the resulting potential output is about -6.96 V(Fig. 3f-h) This COMSOL simulation result demonstrate that the transmission rate of the electrons of BTO could be improved by introducing of Co-N-C, which is benefit to the transfer of charges and resulting in the improvement of piezoelectric property [15]. It also indicates that the combination of Co-N-C and BTO would improve the piezocatalytic performance of the piezocatalysts and show a potential of CO₂RR.

3.2. Piezocatalytic CO₂ reduction reaction

Fig. 4a shows the yield of products of PCO₂RR by Co-N-C@BTO under different ultrasonic frequencies. In the absence of any sacrificial agent, the product components are mainly CO and H₂. It is worth mentioning that under various ultrasonic frequencies, the CO is generated only at 50 kHz. The highest CO yield reached 261.8 $\mu\text{mol g}^{-1}\text{h}^{-1}$, and the CO selectivity also reached 93.8%. Under other frequencies, no CO is detected and only a small amount of H₂ is generated. The CO yields for the PCO₂RR using Co-N-C@BTO piezocatalyst outperform most of the reported photocatalytic CO₂RR and PCO₂RR (Table S5). [31,53,54] This means that PCO₂RR using Co-N-C@BTO piezocatalysts has an excellent application prospect. In addition, in order to exclude the influence of pristine BTO, the blank experiment without any piezocatalyst and the comparison experiment of pristine BTO are employed and only a small amount of H₂ is generated when pristine BTO is subjected to ultrasonic vibration, and no CO is detected (Table S6 and S7). Meanwhile, in the current research on electrocatalysis and photocatalysis in CO₂RR, no reduction of carbon catalysts to CO have been reported [25,30,55]. Some studies have achieved a great catalytic activity in the CO₂RR using pure carbon materials as catalysts and manufacturing intrinsic

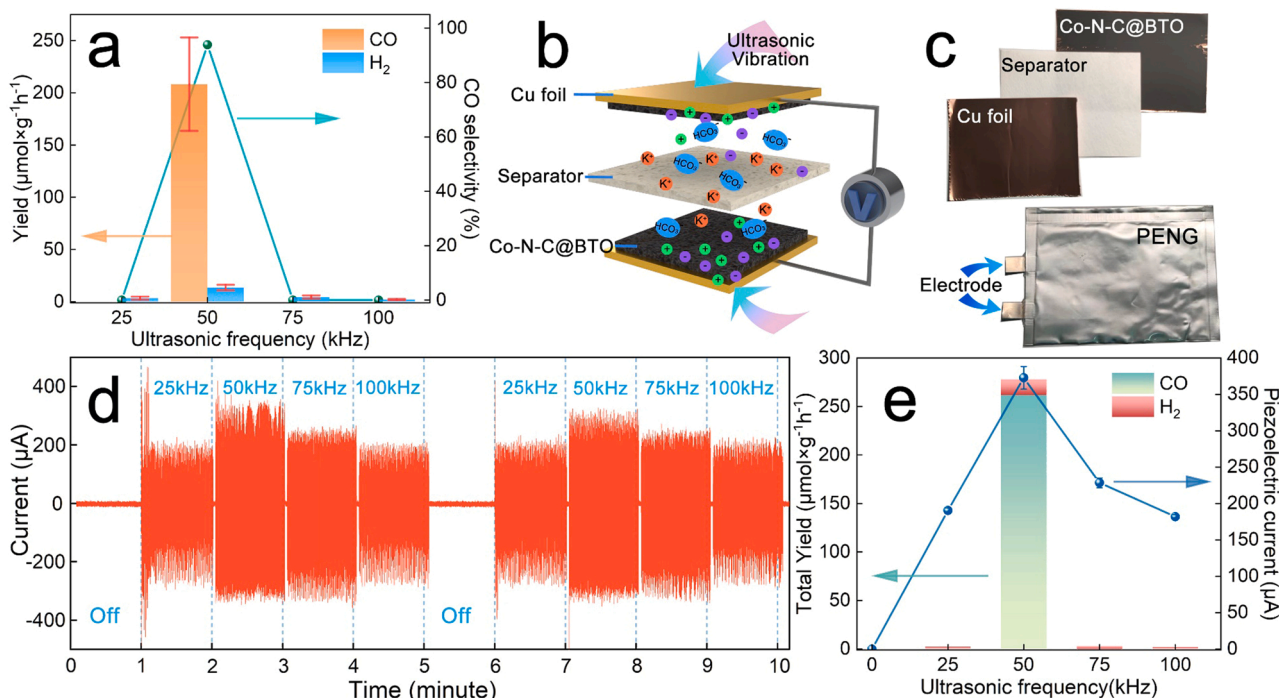


Fig. 4. PCO₂RR and piezoelectric current of Co-N-C@BTO PENG. (a) CO and H₂ yield and CO selectivity with different ultrasonic frequencies for PCO₂RR using Co-N-C@BTO. (b) Schematic of the PENG experimental setup for electrochemical measurement. (c) The image of Co-N-C@BTO PENG. (d) Chronoamperometry curve of Co-N-C@BTO PENG. (e) Piezoelectric current and total gas yield of piezocatalysis.

carbon-defects to improve catalytic activity of CO₂RR [56,57]. These experiments demonstrate the stability of the carbon-based catalyst. Based on current research, it should be hardly that a carbon catalyst will be reduced to CO. For those reasons, this phenomenon indicates that the Co-N-C@BTO piezocatalyst has a superior piezocatalytic activity and selectivity in the PCO₂RR.

3.3. Piezocatalytic mechanism investigation

In order to figure out the piezocatalytic mechanism, this paper combines piezoelectric effect and energy band theory, and innovatively introduces displacement current and the principle of PENG. [13] Meanwhile, a series of experiments and simulation methods are designed to investigate the proposed mechanism. It is generally known that the piezoelectric properties of a crystal are closely related to the asymmetry of its crystal structure. In this paper, BTO is selected as the piezoelectric provider due to its excellent piezoelectric response, which has a cubic unit cell structure at room temperature (Fig. S14). [58,59] The Ba²⁺ ions are located at the eight corners of the cuboid, while O²⁻ ions are located at the six surfaces center of the cuboid, and Ti⁴⁺ ions are situated above (or below) the center of the cuboid. According to the asymmetry characteristic of the crystal structure of BTO, the centers of positive and negative ions are not overlapped. Hence, there is an electric dipole moment along with Z-axis in BTO, and the BTO has spontaneous polarization properties. When mechanical force squeezes BTO, the stretching deformation in the Z-axis leads to the displacement of Ti⁴⁺ ions along the Z-axis to change the electric dipole moment, which generates the piezoelectric effect and accumulates lots of charges on the surface of BTO. [60] However, the accumulated charges will not spontaneously transfer to active sites without a push. To solve this problem, we are inspired by displacement current and the principle of PENG (Figs. 4b, 4c). According to Maxwell's equations:

$$J_D = \frac{\partial D}{\partial t} \quad (1.1)$$

$$D = \epsilon_0 E + P \quad (1.2)$$

$$J_D = \frac{\partial D}{\partial t} = \epsilon_0 \frac{\partial E}{\partial t} + \frac{\partial P}{\partial t} \quad (1.3)$$

where J represents current density, D represents the displacement field, E represents an electric field, ϵ_0 represents vacuum dielectric constant, P represents polarization field density, and t is time.

The second part $\frac{\partial P}{\partial t}$ in Eq. 1.3 represents Maxwell's displacement current. The displacement current is not an electric current of moving charges, but a time-varying electric field (vacuum and media), plus a contribution from the slight motion of charges bound in atoms, dielectric polarization in materials. [13] According to the research on the principle of PENG by Wang et al., [4,6,7,61] the displacement current is the output characteristic of PENG derived from the displacement current inside the piezoelectric material. For the external circuit, the PENG acts like a capacitor, where the time-varying electrostatic potential generated by the piezoelectric polarized charges accumulated on its surface drives the flow of electrons to the external circuit. [13] Therefore, a PENG is designed and assembled by Co-N-C@BTO piezocatalyst (Figs. 4b, 4c). The piezoelectric current response is detected by chronoamperometry (Fig. 4d). There is no piezoelectric current without ultrasonic vibration. It reveals that no displacement current is formed inside the piezoelectric material, thus no time-varying electrostatic potential is formed to drive the electrons to flow into the external circuit. When ultrasonic vibration is applied to the Co-N-C@BTO PENG, a piezoelectric current signal is detected, and the magnitude of the piezoelectric current varies on different ultrasonic frequencies. Under the 50 kHz vibration, the piezoelectric current generated by Co-N-C@BTO PENG is larger than that at other frequencies. Due to the formation of a strong displacement currents inside of BTO and a

powerful time-varying electrostatic potential is formed which results in a stronger piezoelectric current. These results also indicate that the Co-N-C@BTO piezocatalyst should generate a larger number of electrons flowing into the active sites thus facilitating the PCO₂RR under an ultrasonic frequency of 50 kHz. And this phenomenon is also consistent with the CO yield trend of PCO₂RR (Fig. 4e).

However, this phenomenon also brings up an interesting question. Based on the traditional understandings of the piezoelectric effect, the greater the external force is subjected to the piezoelectric material, the stronger piezoelectric current should be generated. [62] Nevertheless, the Co-N-C@BTO PENG piezoelectric current response does not show a linear relationship with the increase of the applied vibration frequency when detecting the piezoelectric current of PENG. Instead, the piezoelectric current of Co-N-C@BTO PENG shows a trend which increases gradually from 25 kHz, reaches a maximum value at 50 kHz and then decreases. We propose that since piezoelectric materials have their own resonant frequency, the piezoelectric material will undergo maximum deformation when the frequency of the external force is close to the resonant frequency. This will generate a larger piezoelectric effect and hence a stronger piezoelectric current. For now, there is no study about our hypothesis. We observed the trend during our experiments and proposed for the first time to validate it using COMSOL simulation method (Fig. 5). We simplify the BTO into a cylindrical model and simulate its performance such as total displacement, maximum voltage, and maximum electrical energy under different vibration frequencies. Based on some parameters of the COMSOL database of BTO and BTO's cylindrical shape, the resonant frequency of BTO cylindrical model is 264 MHz, it is obtained from the result of COMSOL simulation. As is shown in the simulated data (Fig. S15-S17), the maximum displacement (deformation), maximum potential, and maximum electrical energy of the BTO does not show a linear relationship with the vibration frequency. According to the resonance effect, the BTO model will experience maximum displacement (deformation) when subjected to the same applied frequency as its own resonant frequency, resulting in maximum electrical energy. The COMSOL simulation results are dependent on the shape of the model and the direction of the vibrations received. In the COMSOL simulations, the vibrations applied to the model are only in the Z-axis direction. However, in the experiment, the pressure applied to the surface of the piezocatalyst by ultrasonic vibrations can come from all directions at the same time. Meanwhile, the morphology of Co-N-C@BTO piezocatalysts are irregularly after ball milling process, which means more mechanical energy is applied to the piezoelectric catalyst per unit time and stronger piezoelectric effect will be formed. Therefore, although the results of the COMSOL simulations differ from the experimental results in numerical values, the trend is the same for COMSOL simulation and experimental results. Therefore, the resonance effect of the piezocatalyst may explain the volcanic trend of the piezoelectric current of Co-N-C@BTO PENG as a function of frequency. This result indicates that it is not necessary to receive a larger mechanical energy to generate a higher piezoelectric response for the piezocatalyst. Instead, the selection of piezocatalyst should be based on the physical properties of different piezoelectric materials, such as resonance frequency and morphology. Only by selecting the appropriate piezoelectric material can a better piezoelectric response be achieved, thereby achieving the purpose of energy saving.

Previously, the mechanism for piezocatalysis is based on the piezoelectric effect. But the charges generated by the piezoelectric effect are not able to participate spontaneously in the reaction; these charges still need a potential as a driving force. Based on the working principle of PENG and displacement current above-mentioned, the piezoelectric current data can prove the formation of displacement current inside of piezocatalysts. The formation of displacement current inside of piezocatalysts could result in the formation of a time-varying electrostatic potential on the surface of it. Owing to the equation of displacement current, the second term of $\frac{\partial P}{\partial t}$ from the Maxwell equations (Eq. 1.3), the

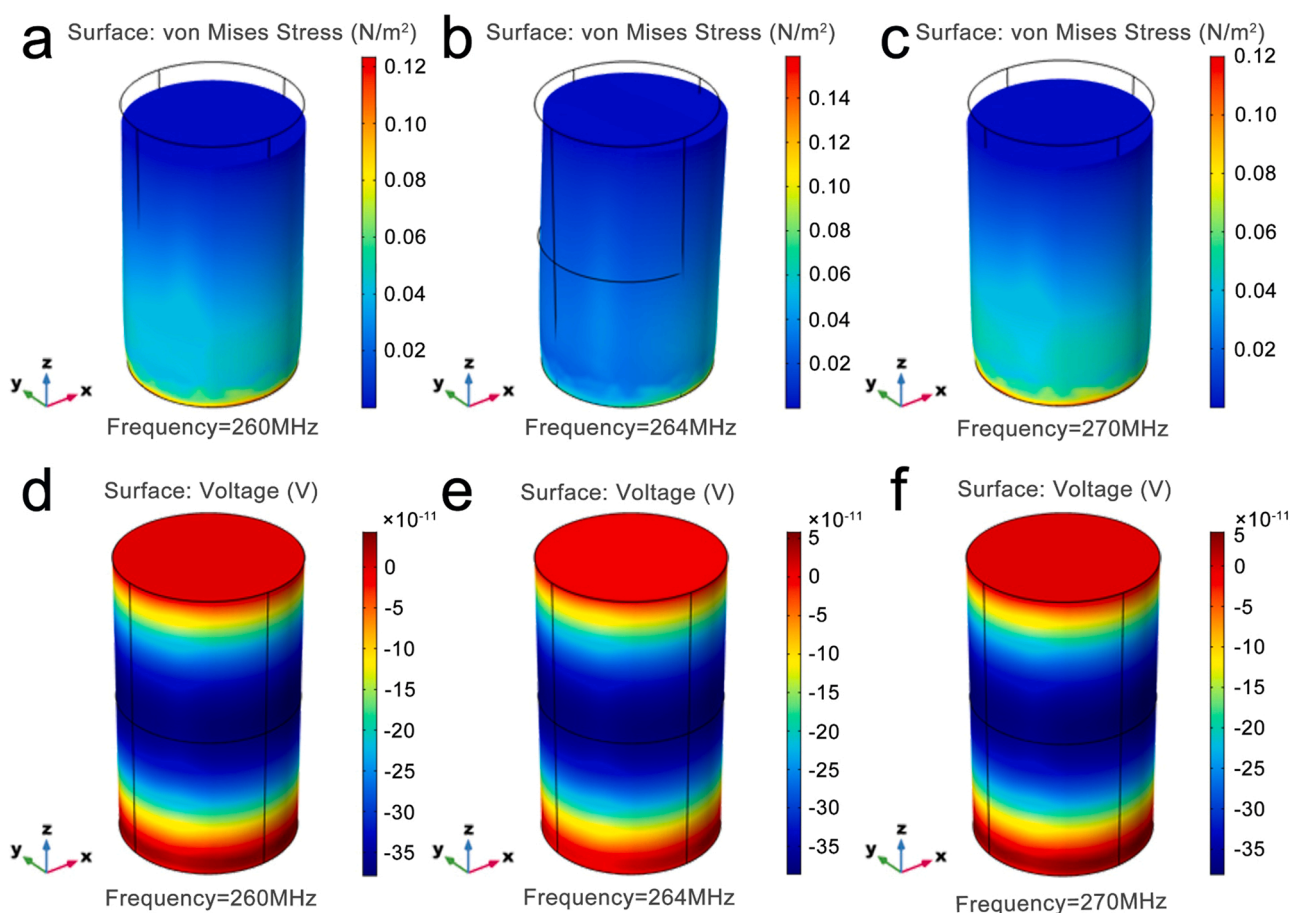


Fig. 5. The von Miss stress and piezoelectric potential of BTO under different frequencies by COMSOL simulation. (a-c) The von Mises stress on BTO under different frequencies (260 MHz, 264 Mhz, and 270 MHz). (d-f) The piezoelectric voltage on the surface of BTO under different frequencies (260 MHz, 264 MHz, and 270 MHz).

∂t means that the displacement current is a time-varying process under ultrasonic vibration. If there is no change in the pressure applied to the piezoelectric catalyst, then the displacement current will not form. Without displacement current, there are no time-varying electrostatic potential. Without a time-varying electrostatic potential, there are no piezocatalysis could occur. The process of ultrasonic microbubble generation satisfies this condition. The creation and bursting of microbubbles can provide a time-varying pressure on the piezocatalyst [63–65]. Therefore, the generation of displacement currents and time-varying electrostatic potential are dynamic process. Meanwhile, based on the energy band theory, the energy band structure of piezocatalyst needs to satisfy the potential required for the reaction. Hence, the displacement current would form during the ultrasonic vibration inside of piezocatalyst, and result in the formation of a time-varying electrostatic potential to drive the electrons to the active sites to participate in the reaction.

For the reason we have discussed above, the piezocatalyst forms a time-varying electrostatic potential under ultrasonic vibration, and it is the driving force that drives the electrons which are generated by piezoelectric effect and accumulated on the surface of the piezoelectric material. At the same time, the energy band structure of the BTO satisfies the potential requirement for CO₂RR, then electrons will flow to the active sites driven by the time-varying electrostatic potential to participate in the reaction. In order to achieve the potential requirements of CO₂RR, the piezoelectric material needs to have a suitable energy band structure, and its conduction band (CB) position should be more negative than the potential of CO₂RR to promote the reduction reaction. Therefore, the energy band structures of BTO, Co-N-C, and Co-

N-C@BTO are determined by the combination of UV–vis diffuse reflectance spectra and Mott–Schottky curves. According to the UV–vis diffuse reflectance spectrum (Fig. 6a), the semiconductor properties and band gaps of BTO and Co-N-C@BTO are revealed by the Tauc plot method. The calculation equation of the Tauc plot is as follows:

$$(\alpha h\nu)^{\frac{1}{n}} = A(h\nu - E_g) \quad (1.4)$$

where α , h , ν , and E_g are the absorption coefficient, Plank constant, frequency, and band gap, respectively. A is a constant and n is 1/2 considering that BTO is a directly band gap semiconductor.

According to the tangent line for $(\alpha h\nu)^2$ versus $h\nu$ (inset of Fig. 6a), the band gap of BTO is calculated as 3.19 eV. The positive slope of the Mott–Schottky curves reveals that the BTO shows n-type semiconductor properties, and the flat band potential of BTO, Co-N-C, and Co-N-C@BTO are -1.076 V, -0.427 V, and -0.949 V versus the Ag/AgCl electrode (vs. Ag/AgCl), respectively (Fig. 6b). The Fermi level of BTO, Co-N-C and Co-N-C@BTO versus the reversible hydrogen electrode (vs. RHE) are acquired by the Equation S1.0 to be -0.365 V, 0.283 V and -0.238 V (vs. RHE), respectively. Semiconductor energy band structure data is illustrated in Table S8 and Table S18. Based on the data above, the energy band structures of BTO and Co-N-C@BTO are illustrated in Fig. 6c. As BTO is an n-type semiconductor, its Fermi level is near the CB. The CB position of BTO is calculated as about -0.67 V. Meanwhile, the valance band (VB) position of BTO is 2.53 V according to the band gap [52,66]. As we can see from Fig. S18, the Fermi energy level of BTO as an n-type semiconductor is higher than that of Co-N-C. Meanwhile, the Co-N-C work function (φ_m) is greater than the electron affinity energy (χ) of BTO which means that a Schottky-barrier is formed between the

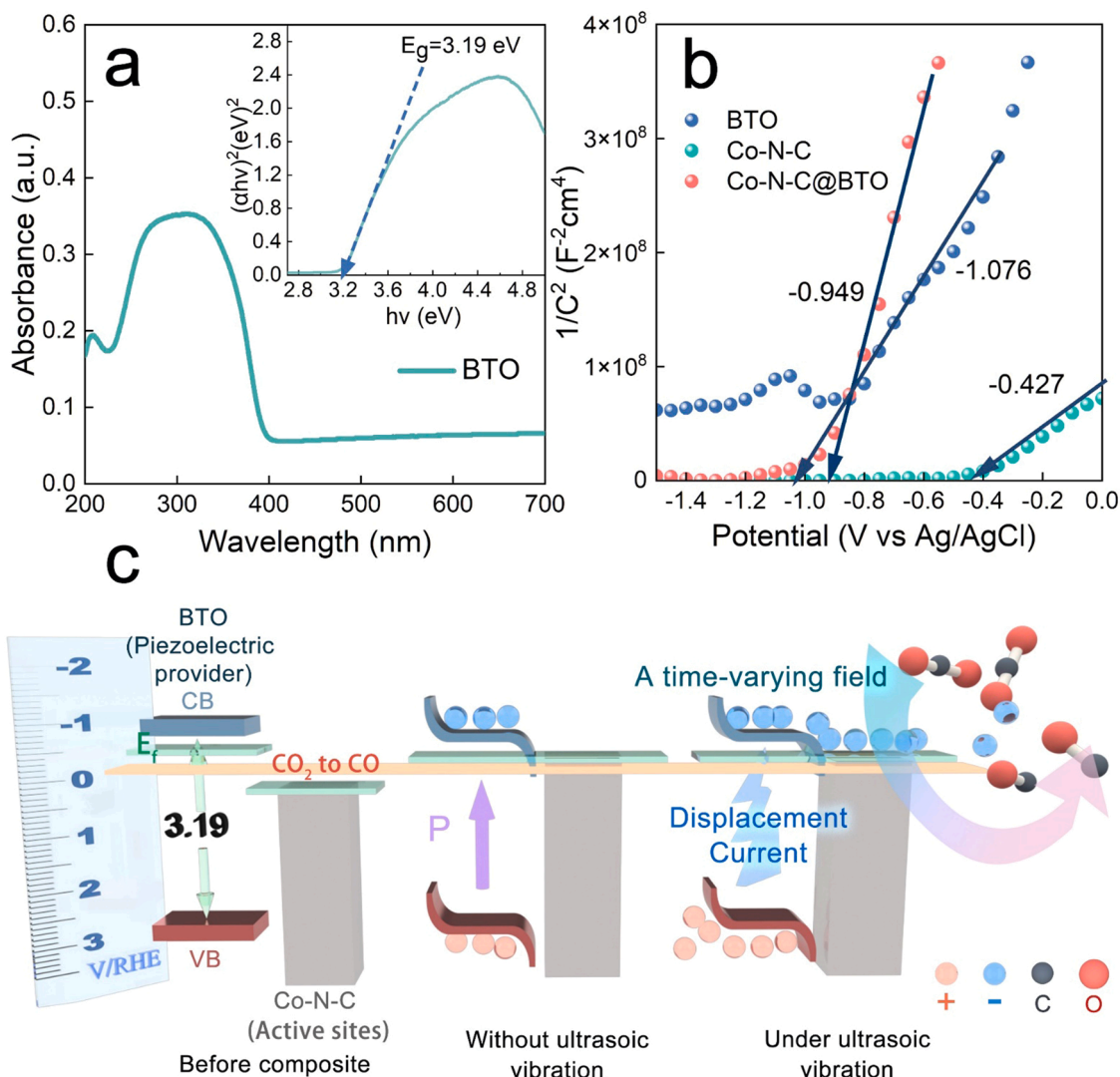
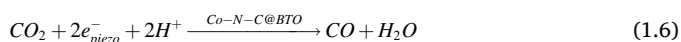
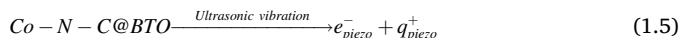


Fig. 6. The structure of the semiconductor energy band of BTO and Co-N-C@BTO. (a) The solid UV-vis diffuse reflectance spectra and E_g of BTO. (b) The Mott-Schottky plots of BTO, Co-N-C and Co-N-C@BTO. (c) the semiconductor energy band structure of Co-N-C@BTO and PCO_2RR reaction schematic diagram.

Co-N-C and BTO [67,68]. After being composited with Co-N-C, the overall Fermi level and band energy of Co-N-C@BTO is declined because of the formation of the Schottky-barrier between the BTO and Co-N-C. Meanwhile, the introduction of Co-N-C could enhance the electrons transfer efficiency of BTO thus boost the piezoelectric properties and piezocatalytic performance.



The CB position of BTO is more negative than the potential of CO_2 reduction to CO (-0.106 V vs. RHE). [25] It is possible for the electrons to drive the CO_2RR when a time-varying electrostatic potential is formed due to the displacement current under ultrasonic vibration. The electrons transfer from the BTO to Co-N-C to accomplish the CO_2RR as shown in Eqs. 1.5 and 1.6.

And about the source of electrons, in this paper, we believe that the electrons are generated by piezoelectric effect, because not all the piezoelectric material have a semiconductor nature. Even the BTO is chosen to be a piezoelectric provider in this study, we prefer to choose a widely received and more reasonable theory (piezoelectric effect) to explain the source of electrons, because the piezoelectric effect will not

be limited by its semiconductor nature.

To sum up, a comprehensive understanding of the piezocatalytic mechanism is presented from displacement current to active sites. Under 50 kHz ultrasonic vibration frequency, ultrasonic bubbles will continue to generate and the burst of ultrasonic bubbles will provide a time-varying pressure in the solution. Based on displacement current theory and working principle of PENG, the displacement current is formed inside the BTO, thus creating a time-varying electrostatic potential on its surface. The time-varying electrostatic potential drives the flow of electrons which generated by piezoelectric effect and accumulated on the surface of the BTO to the Co-N-C. The energy band structure of BTO satisfies the reduction potential of CO_2 to CO. The piezocatalysis process is completed for the reason mentioned-above.

Based on the above mechanism, when designing piezocatalysts in the future, piezoelectric semiconductor materials with suitable energy band structure and larger piezoelectric coefficient should be selected according to the reduction potential of the probe reaction. Meanwhile, the active sites with excellent activity and selectivity should be selected with the reference to photocatalysts and electrocatalysts. In addition, owing to the different types and morphologies of piezocatalysts have different responses to mechanical energy, lead-free piezoelectric materials with lower resonance frequencies should be selected for more energy-saving and environmental protection, and their morphologies should be

adjusted to absorb mechanical energy more efficiently.

4. Conclusions

In this work, we successfully synthesize a Co-N-C@BTO piezocatalyst for the efficient PCO₂RR. Under the ultrasonic frequency of 50 kHz, the maximum CO yield (261.8 $\mu\text{mol g}^{-1}\text{h}^{-1}$) is achieved with a high CO selectivity up to 93.8%, which outperforms most of the reported photocatalytic CO₂RR and PCO₂RR. Moreover, this work innovatively introduces the displacement current and the principle of PENG to comprehensively describe the piezocatalytic mechanism while combining the piezoelectric effect and energy band theory. By employing PENG, COMSOL simulation, and energy band structure analysis, a more insightful explanation for the piezocatalysis is revealed from displacement current to active sites. A time-varying mechanical force applied to the piezocatalyst is the key to the piezocatalytic reaction. According to displacement current theory, it is the time-varying mechanical forces that trigger the formation of displacement currents within the piezocatalyst, which creates a time-varying electrostatic potential. The time-varying electrostatic potential generated by the displacement current is the driving force for electrons transfer, which drives electrons generated by the piezoelectric effect from BTO to Co-N-C. The band structure of BTO satisfies the reaction potential to facilitate electrons to accomplish CO₂RR upon active sites. Meanwhile, the piezoelectric current and COMSOL simulation also reveals that the piezoelectric material will deform more and excite a stronger piezoelectric effect when the vibration frequency is close to the resonance frequency of the piezoelectric material itself due to the resonance effect. This also indicates that piezocatalysis does not necessarily apply larger mechanical energy to promote catalytic activity. Selecting piezoelectric materials with lower resonance frequencies to prepare a high-efficiency absorbing mechanical energy morphology will be more beneficial to energy-saving and high piezocatalytic performance. Furthermore, the design of piezocatalysts based on the above mechanism is expected to provide a feasible way to enhance the piezocatalytic performance. According to the requirements of probe reactions, piezoelectric semiconductor materials with large piezoelectric response (higher piezoelectric coefficients, lower resonant frequency and appropriate morphology for the efficient mechanical energy absorption) and a suitable energy band structure should be selected as piezoelectric providers. Meanwhile, the active sites with excellent activity and selectivity should be selected with the reference to photocatalysts and electrocatalysts. The piezocatalytic mechanisms and design of piezocatalysts can be extended to other piezocatalytic reactions, such as degradation reaction, hydrogen production reaction, and organic synthesis. With the increasingly prominent energy crisis, efficient piezocatalysis will provide more opportunities and possibilities for realizing energy saving, environmental protection and carbon recycling.

CRedit authorship contribution statement

Zhuoran Ren: Conceptualization, Mechanism, Methodology, Software, Investigation, Formal analysis, Writing – original draft, Writing – review & editing; **Fang Chen:** Software, Methodology; **Qin Zhao:** Writing – review & editing; **Guoqiang Zhao:** Investigation; **Hui Li:** Software; **Wenping Sun:** Writing – review & editing; **Hongwei Huang:** Writing – review & editing; **Tianyi Ma:** Funding acquisition, Writing – review & editing.

Declaration of Competing Interest

The authors declare that they have no known competing financial interests or personal relationships that could have appeared to influence the work reported in this paper.

Data availability

Data will be made available on request.

Acknowledgments

This work was supported by the National Natural Science Foundation of China (No. 52071171, 22109060, 52202248), Liaoning Revitalization Talents Program - Pan Deng Scholars (XLYC1802005), Liaoning BaiQianWan Talents Program (LNBQW2018B0048), Natural Science Fund of Liaoning Province for Excellent Young Scholars (2019-YQ-04), Key Project of Scientific Research of the Education Department of Liaoning Province (LZD201902), Shenyang Science and Technology Project (21-108-9-04), Research Fund for the Doctoral Program of Liaoning Province (2020-BS-085), the 2021 Annual Scientific Research Funding Project of the Educational Department of Liaoning Province (LJKZ0101), the Scientific Research Startup Project of Baotou Teachers' College (01108022/035), Australian Research Council (ARC) through Future Fellowship (FT210100298), Discovery Project (DP220100603) and Linkage Project (LP210200504) schemes, CSIRO Energy Centre and Kick-Start Project. The Study Melbourne Research Partnerships program has been made possible by funding from the Victorian Government through Study Melbourne.

Appendix A. Supporting information

Supplementary data associated with this article can be found in the online version at doi:10.1016/j.apcatb.2022.122007.

References

- [1] A century of ferroelectricity, *Nat. Mater.*, 19 (2020) 129.
- [2] S. Li, Z. Zhao, J. Zhao, Z. Zhang, X. Li, J. Zhang, Recent advances of ferro-, piezo-, and pyroelectric nanomaterials for catalytic applications, *ACS, Appl. Nano Mater.* 3 (2020) 1063–1079.
- [3] S. Tu, Y. Guo, Y. Zhang, C. Hu, T. Zhang, T. Ma, H. Huang, Piezocatalysis and piezo-photocatalysis: catalysts classification and modification strategy, reaction mechanism, and practical application, *Adv. Funct. Mater.* 30 (2020), 2005158.
- [4] Z.L. Wang, J. Song, Piezoelectric nanogenerators based on zinc oxide nanowire arrays, *Science* 312 (2006) 242–246.
- [5] S.-F. Leung, H.-C. Fu, M. Zhang, A.H. Hassan, T. Jiang, K.N. Salama, Z.L. Wang, J.-H. He, Blue energy fuels: converting ocean wave energy to carbon-based liquid fuels via CO₂ reduction, *Energy Environ. Sci.* 13 (2020) 1300–1308.
- [6] Y. Xi, J. Wang, Y. Zi, X. Li, C. Han, X. Cao, C. Hu, Z. Wang, High efficient harvesting of underwater ultrasonic wave energy by triboelectric nanogenerator, *Nano Energy* 38 (2017) 101–108.
- [7] W. Xu, H. Zheng, Y. Liu, X. Zhou, C. Zhang, Y. Song, X. Deng, M. Leung, Z. Yang, R. X. Xu, Z.L. Wang, X.C. Zeng, Z. Wang, A droplet-based electricity generator with high instantaneous power density, *Nature* 578 (2020) 392–396.
- [8] F. Meng, W. Ma, Y. Wang, Z. Zhu, Z. Chen, G. Lu, A tribo-positive Fe@MoS₂ piezocatalyst for the durable degradation of tetracycline: degradation mechanism and toxicity assessment, *Environ. Sci.: Nano* 7 (2020) 1704–1718.
- [9] B. Ghatak, S. Banerjee, S.B. Ali, R. Bandyopadhyay, N. Das, D. Mandal, B. Tudu, Design of a self-powered triboelectric face mask, *Nano Energy* 79 (2021), 105387.
- [10] W. Qian, W. Yang, Y. Zhang, C.R. Bowen, Y. Yang, Piezoelectric materials for controlling electro-chemical processes, *Nano-Micro Lett.* 12 (2020) 149.
- [11] K. Wang, C. Han, J. Li, J. Qiu, J. Sunarso, S. Liu, The Mechanism of Piezocatalysis: Energy Band Theory or Screening Charge Effect? *Angew. Chem. Int. Ed.* 61 (2021) 2–15.
- [12] Daiming Liu, Yawei Song, Zhijie Xin, Guoxia Liu, Chengchao Jin, F. Shan, High-piezocatalytic performance of eco-friendly (Bi_{1/2}Na_{1/2})TiO₃-based nanofibers by electrospinning, *Nano Energy* 65 (2019), 104024.
- [13] Z.L. Wang, On Maxwell's displacement current for energy and sensors: the origin of nanogenerators, *Mater. Today* 20 (2017) 74–82.
- [14] A. Biswas, S. Saha, N.R. Jana, ZnSnO₃ nanoparticle-based piezocatalysts for ultrasound-assisted degradation of organic pollutants, *ACS Appl. Nano Mater.* 2 (2019) 1120–1128.
- [15] G. Yang, Q. Chen, W. Wang, S. Wu, B. Gao, Y. Xu, Z. Chen, S. Zhong, J. Chen, S. Bai, Cocatalyst engineering in piezocatalysis: a promising strategy for boosting hydrogen evolution, *ACS Appl. Mater. Interfaces* 13 (2021) 15305–15314.
- [16] F. Xu, Z. Li, R. Zhu, Y. Chu, Z. Pan, S. Xia, J. Fu, Z. Xiao, X. Ji, M. Liu, B. Weng, Narrow band-gapped perovskite oxysulfide for CO₂ photoreduction towards ethane, *Appl. Catal. B-Environ.* 316 (2022), 121615.
- [17] S. Cha, S.M. Kim, H. Kim, J. Ku, J.I. Sohn, Y.J. Park, B.G. Song, M.H. Jung, E.K. Lee, B.L. Choi, J.J. Park, Z.L. Wang, J.M. Kim, K. Kim, Porous PVDF as effective sonic wave driven nanogenerators, *Nano Lett.* 11 (2011) 5142–5147.

- [18] L. Yang, Q. Zhao, K. Chen, Y. Ma, Y. Wu, H. Ji, J. Qiu, PVDF-based composition-gradient multilayered nanocomposites for flexible high-performance piezoelectric nanogenerators, *ACS Appl. Mater. Interfaces* 12 (2020) 11045–11054.
- [19] Y. Feng, L. Ling, Y. Wang, Z. Xu, F. Cao, H. Li, Z. Bian, Engineering spherical lead zirconate titanate to explore the essence of piezo-catalysis, *Nano Energy* 40 (2017) 481–486.
- [20] D. Liu, C. Jin, F. Shan, J. He, F. Wang, Synthesizing BaTiO₃ nanostructures to explore morphological influence, kinetics, and mechanism of piezocatalytic dye degradation, *ACS Appl. Mater. Interfaces* 12 (2020) 17443–17451.
- [21] J. Ma, J. Ren, Y. Jia, Z. Wu, L. Chen, N.O. Haugen, H. Huang, Y. Liu, High efficiency bi-harvesting light/vibration energy using piezoelectric zinc oxide nanorods for dye decomposition, *Nano Energy* 62 (2019) 376–383.
- [22] Y. Cai, Y. Zhang, Z. Lv, S. Zhang, F. Gao, M. Fang, M. Kong, P. Liu, X. Tan, B. Hu, X. Wang, Highly efficient uranium extraction by a piezo catalytic reduction-oxidation process, *Appl. Catal. B-Environ.* 310 (2022), 121343.
- [23] J. Hu, Y. Chen, Y. Zhou, L. Zeng, Y. Huang, S. Lan, M. Zhu, Piezo-enhanced charge carrier separation over plasmonic Au-BiOBr for piezo-photocatalytic carbamazepine removal, *Appl. Catal. B-Environ.* 311 (2022), 121369.
- [24] E. Lin, Z. Kang, J. Wu, R. Huang, N. Qin, D. Bao, BaTiO₃ nanocubes/cuboids with selectively deposited Ag nanoparticles: efficient piezocatalytic degradation and mechanism, *Appl. Catal. B-Environ.* 285 (2021), 119823.
- [25] M.B. Ross, P. De Luna, Y. Li, C.-T. Dinh, D. Kim, P. Yang, E.H. Sargent, Designing materials for electrochemical carbon dioxide recycling, *Nat. Catal.* 2 (2019) 648–658.
- [26] S. Nitopi, E. Bertheussen, S.B. Scott, X. Liu, A.K. Engstfeld, S. Horch, B. Seger, I.E. L. Stephens, K. Chan, C. Hahn, J.K. Nørskov, T.F. Jaramillo, I. Chorkendorff, Progress and perspectives of electrochemical CO₂ reduction on copper in aqueous electrolyte, *Chem. Rev.* 119 (2019) 7610–7672.
- [27] S. Das, J. Perez-Ramirez, J. Gong, N. Dewangan, K. Hidajat, B.C. Gates, S. Kawi, Core-shell structured catalysts for thermocatalytic, photocatalytic, and electrocatalytic conversion of CO₂, *Chem. Soc. Rev.* 49 (2020) 2937–3004.
- [28] B.M. Tackett, E. Gomez, J.G. Chen, Net reduction of CO₂ via its thermocatalytic and electrocatalytic transformation reactions in standard and hybrid processes, *Nat. Catal.* 2 (2019) 381–386.
- [29] Y.Y. Birdja, E. Pérez-Gallent, M.C. Figueiredo, A.J. Göttele, F. Calle-Vallejo, M.T. M. Koper, Advances and challenges in understanding the electrocatalytic conversion of carbon dioxide to fuels, *Nat. Energy* 4 (2019) 732–745.
- [30] S.E. Renfrew, D.E. Starr, P. Strasser, Electrochemical approaches toward CO₂ capture and concentration, *ACS Catal.* 10 (2020) 13058–13074.
- [31] W. Zhang, A.R. Mohamed, W.J. Ong, Z-scheme photocatalytic systems for carbon dioxide reduction: where are we now? *Angew. Chem. Int. Ed.* 59 (2020) 22894–22915.
- [32] Y. Li, G. Shi, T. Chen, L. Zhu, D. Yu, Y. Sun, F. Besenbacher, M. Yu, Simultaneous increase of conductivity, active sites and structural strain by nitrogen injection for high-yield CO₂ electro-hydrogenation to liquid fuel, *Appl. Catal. B-Environ.* 305 (2022), 121080.
- [33] M. Yang, P. Wang, Y. Li, S. Tang, X. Lin, H. Zhang, Z. Zhu, F. Chen, Graphene aerogel-based NiAl-LDH/g-C₃N₄ with ultratight sheet-sheet heterojunction for excellent visible-light photocatalytic activity of CO₂ reduction, *Appl. Catal. B-Environ.* 306 (2022), 121065.
- [34] Y. Chen, X. Li, J. Zhang, N. Zhao, L. Dai, X. Jiang, C. Liu, S. Lyu, Z. Li, Preparation of SiO₂ immobilized Co-based catalysts from ZIF-67 and the enhancement effect for Fischer-Tropsch synthesis, *Appl. Catal. B-Environ.* 289 (2021), 120027.
- [35] P.V. Kamat, S. Jin, Semiconductor Photocatalysis: “Tell Us the Complete Story!”, *ACS Energy Lett.* 3 (2018) 622–623.
- [36] A. Kudo, Y. Miseki, Heterogeneous photocatalyst materials for water splitting, *Chem. Soc. Rev.* 38 (2009) 253–278.
- [37] L. He, W. Zhang, S. Liu, Y. Zhao, Three-dimensional porous N-doped graphitic carbon framework with embedded CoO for photocatalytic CO₂ reduction, *Appl. Catal. B-Environ.* 298 (2021), 120546.
- [38] Y. Wei, Y. Li, M. Wu, Y. Li, The decomposition of total-factor CO₂ emission efficiency of 97 contracting countries in Paris Agreement, *Energy Econ.* 78 (2019) 365–378.
- [39] X. Wang, Z. Chen, X. Zhao, T. Yao, W. Chen, R. You, C. Zhao, G. Wu, J. Wang, W. Huang, J. Yang, X. Hong, S. Wei, Y. Wu, Y. Li, Regulation of coordination number over single Co sites: triggering the efficient electroreduction of CO₂, *Angew. Chem. Int. Ed.* 57 (2018) 1944–1948.
- [40] P. Yin, T. Yao, Y. Wu, L. Zheng, Y. Lin, W. Liu, H. Ju, J. Zhu, X. Hong, Z. Deng, G. Zhou, S. Wei, Y. Li, Single cobalt atoms with precise N-coordination as superior oxygen reduction reaction, *Catal.*, *Angew. Chem. Int. Ed.* 55 (2016) 10800–10805.
- [41] E. Lin, J. Wu, N. Qin, B. Yuan, D. Bao, Silver modified barium titanate as a highly efficient piezocatalyst, *Catal. Sci. Technol.* 8 (2018) 4788–4796.
- [42] C. Jin, D. Liu, J. Hu, Y. Wang, Q. Zhang, L. Lv, F. Zhuge, The role of microstructure in piezocatalytic degradation of organic dye pollutants in wastewater, *Nano Energy* 59 (2019) 372–379.
- [43] P.T.T. Phuong, D.-V.N. Vo, N.P.H. Duy, H. Pearce, Z.M. Tsikriteas, E. Roake, C. Bowen, H. Khanbarez, Piezoelectric catalysis for efficient reduction of CO₂ using lead-free ferroelectric particulates, *Nano Energy* 95 (2022), 107032.
- [44] X. Li, W. He, C. Li, B. Song, S. Liu, Synergetic surface modulation of ZnO/Pt@ZIF-8 hybrid nanorods for enhanced photocatalytic CO₂ valorization, *Appl. Catal. B-Environ.* 287 (2021), 119934.
- [45] W. Pei, J. Zhang, H. Tong, M. Ding, F. Shi, R. Wang, Y. Huo, H. Li, Removal and reutilization of metal ions on ZIF-67/GO membrane via synergistic photocatalytic-photothermal route, *Appl. Catal. B-Environ.* 282 (2021), 119575.
- [46] R. Eguchi, S. Uchida, N. Mizuno, Highly Selective Sorption and Separation of CO₂ from a Gas Mixture of CO₂ and CH₄ at Room Temperature by a Zeolitic Organic-Inorganic Ionic Crystal and Investigation of the Interaction with CO₂, *J. Phys. Chem. C* 116 (2012) 16105–16110.
- [47] K. Morishige, Adsorption and separation of CO₂/CH₄ on amorphous silica molecular sieve, *J. Phys. Chem. C* 115 (2011) 9713–9718.
- [48] Y. Li, S.L. Zhang, W. Cheng, Y. Chen, D. Luan, S. Gao, X.W. Lou, Loading single-Ni atoms on assembled hollow n-rich carbon plates for efficient CO₂ electroreduction, *Adv. Mater.* 34 (2021), 2105204.
- [49] X. Chen, L. Yu, S. Wang, D. Deng, X. Bao, Highly active and stable single iron site confined in graphene nanosheets for oxygen reduction reaction, *Nano Energy* 32 (2017) 353–358.
- [50] D. Deng, X. Chen, L. Yu, X. Wu, Q. Liu, Y. Liu, A single iron site confined in a graphene matrix for the catalytic oxidation of benzene at room temperature, *Sci. Adv.* 1 (2015), e1500462.
- [51] X. Guo, G. Zhang, G. Li, H. Ma, H. Fan, L. Yu, C. Ma, X. Wu, D. Deng, M. Wei, D. Tan, R. Si, S. Zhang, J. Li, L. Sun, Z. Tang, X. Pan, X. Bao, Direct, nonoxidative conversion of methane to ethylene, aromatics, and hydrogen, *Science* 344 (2014) 616–619.
- [52] X. Zhou, S. Wu, C. Li, F. Yan, H. Bai, B. Shen, H. Zeng, J. Zhai, Piezophototronic effect in enhancing charge carrier separation and transfer in ZnO/BaTiO₃ heterostructures for high-efficiency catalytic oxidation, *Nano Energy* 66 (2019), 104127.
- [53] J. Fu, K. Jiang, X. Qiu, J. Yu, M. Liu, Product selectivity of photocatalytic CO₂ reduction reactions, *Mater. Today* 32 (2020) 222–243.
- [54] F. Chen, T. Ma, T. Zhang, Y. Zhang, H. Huang, Atomic-level charge separation strategies in semiconductor-based photocatalysts, *Adv. Mater.* 33 (2021), e2005256.
- [55] F.-Y. Gao, R.-C. Bao, M.-R. Gao, S.-H. Yu, Electrochemical CO₂-to-CO conversion: electrocatalysts, electrolytes, and electrolyzers, *J. Mater. Chem. A* 8 (2020) 15458–15478.
- [56] W. Wang, L. Shang, G. Chang, C. Yan, R. Shi, Y. Zhao, G.L.N. Waterhouse, D. Yang, T. Zhang, Intrinsic carbon-defect-driven electrocatalytic reduction of carbon dioxide, *Adv. Mater.* 31 (2019), e1808276.
- [57] T. Zheng, K. Jiang, N. Ta, Y. Hu, J. Zeng, J. Liu, H. Wang, Large-scale and highly selective CO₂ electrocatalytic reduction on nickel single-atom catalyst, *Joule* 3 (2019) 265–278.
- [58] D. Berlincourt, H. Jaffe, Elastic and piezoelectric coefficients of single-crystal barium titanate, *Phys. Rev.* 111 (1958) 143–148.
- [59] T. Sakthivel, G. Venugopal, A. Durairaj, S. Vasanthkumar, X. Huang, Utilization of the internal electric field in semiconductor photocatalysis: A short review, *J. Ind. Eng. Chem.* 72 (2019) 18–30.
- [60] Z.L. Wang, Nanopiezotronics, *Adv. Mater.* 19 (2007) 889–892.
- [61] J. Jiao, Q. Lu, Z. Wang, Y. Qin, X. Cao, Sandwich as a triboelectric nanogenerator, *Nano Energy* 79 (2021), 2005158.
- [62] H. Parangusan, D. Ponnamm, M.A.A. Al-Maadeed, Stretchable electrospun PVDF-HFP/Co-ZnO nanofibers as piezoelectric nanogenerators, *Sci. Rep.* 8 (2018) 19813.
- [63] L. Jin, W. Wang, Y. Tu, K. Zhang, Z. Lv, Effect of ultrasonic standing waves on flotation bubbles, *Ultrason. Sonochem.* 73 (2021), 105459.
- [64] S. Behnia, M. Yahyavi, R. Habibpourbisafar, Association schemes perspective of microbubble cluster in ultrasonic fields, *Ultrason. Sonochem.* 44 (2018) 45–52.
- [65] L. Bai, P. Wu, H. Liu, J. Yan, C. Su, C. Li, Rod-shaped cavitation bubble structure in ultrasonic field, *Ultrason. Sonochem.* 44 (2018) 184–195.
- [66] X. Gao, K. Gao, F. Fu, C. Liang, Q. Li, J. Liu, L. Gao, Y. Zhu, Synergistic introducing of oxygen vacancies and hybrid of organic semiconductor: realizing deep structure modulation on Bi₂O₃/I for high-efficiency photocatalytic pollutant oxidation, *Appl. Catal. B-Environ.* 265 (2020), 118562.
- [67] G. Yang, Q. Chen, W. Wang, S. Wu, B. Gao, Y. Xu, Z. Chen, S. Zhong, J. Chen, S. Bai, Cocatalyst engineering in piezocatalysis: a promising strategy for boosting hydrogen evolution, *ACS Appl. Mater. Interfaces* 13 (2021) 15305–15314.
- [68] D. Skachkov, S.-L. Liu, Y. Wang, X.-G. Zhang, H.-P. Cheng, First-principles theory for Schottky barrier physics, *Phys. Rev. B* 104 (2021), 045429.